Research Square

Preprints are preliminary reports that have not undergone peer review.
They should not be considered conclusive, used to inform clinical practice,
or referenced by the media as validated information.

Enhanced Energy Storage Performance and Relaxor Behavior in $CaZrO_3$-Modified $0.76Bi_{0.5}Na_{0.5}TiO_3$-$0.24Sr_{0.7}La_{0.2}TiO_3$ Lead-Free Ceramics

Xiaofan Zheng
Huangshan University
Shuyue Teng
Shenyang University of Chemical Technology
Chong Li
Shenyang University of Chemical Technology
Nianshun Zhao
289177074@qq.com
Huangshan University
Mile Wei
Huangshan University
Juan Hu
Huangshan University
Huanghuang Jin
Huangshan University
Qin Gao
Huangshan University

Research Article

Keywords: Energy storage, Polar nanoregions, Breakdown field strength

Posted Date: May 28th, 2026

DOI: https://doi.org/10.21203/rs.3.rs-9649823/v1

License: This work is licensed under a Creative Commons Attribution 4.0 International License.
Read Full License

Additional Declarations: No competing interests reported.

Version of Record: A version of this preprint was published at Journal of Materials Science: Materials in Electronics on July 23rd, 2026. See the published version at https://doi.org/10.1007/s10854-026-18065-3.

Abstract

In pursuit of lead-free dielectric materials possessing superior energy density and outstanding reliability under intermediate electric field conditions, this study fabricated (1-*x*)($0.76Bi_{0.5}Na_{0.5}TiO_3$-$0.24Sr_{0.7}La_{0.2}TiO_3$)-*x*$CaZrO_3$ (BNSLT-*x*CZ; *x* = 0.00, 0.05, 0.10, 0.15) relaxor ferroelectrics via the classic solid-state ceramic processing. This study systematically explore**s** how $CaZrO_3$ (CZ) incorporation modulates the phase development, microstructural features, dielectric response, and energy storage capabilities. XRD patterns verify the formation of a single-phase perovskite structure, indicating that CZ has been successfully integrated into the BNSLT host lattice without any visible impurities. The evolution of a tripartite phase system—comprising cubic, rhombohedral, and tetragonal symmetries—is facilitated by optimal substitution (*x* = 0.10–0.15). With the suppression of macro-domain ferroelectric order, the formation of polar nanoregions (PNRs) is effectively facilitated, which subsequently enhances the dielectric relaxation response. Noticeably, the *x* = 0.10 composition achieves a high recoverable energy storage density (W_{rec}) of 2.91 J/cm^3 at a modest electric field of 230 kV/cm, with an efficiency (*η)* of 64.3% and a maximum polarization (P_{max}) of 37.8 μC/cm^2. Furthermore, the ceramic demonstrates excellent thermal stability (with W_{rec} variation < ± 10% from 30 to 150°C) and robust frequency stability (from 5 to 100 Hz) under a fixed field of 180 kV/cm, surpassing many reported lead-free systems operating at similar field levels. These results demonstrate that CZ doping enables the synergistic optimization of phase composition and microstructure, providing a promising strategy for emerging micro-scale energy storage devices.

1 Introduction

Driven by the swift progression of electronic devices toward micro-scale integration, high integration, and low power consumption, securing high-capacity energy storage under reduced driving electric fields has emerged as a pivotal challenge for dielectric energy storage materials [1]. Generally, the W, $\mathrm{W}_{\mathrm{rec}}$, and *η* of ceramics can be calculated using the following equations [2]:

$$W_{\mathrm{total}} = \int_0^{P_m} EdP$$

1

$$W_{rec} = \int_{P_r}^{P_m} EdP$$

2

$$\eta = \frac{W_{rec}}{W_{total}} \times 100\% \quad (3)$$

Driven by the demand for eco-friendly electronics, lead-free relaxor ferroelectric ceramics have attracted significant attention as alternatives to lead-based counterparts, principally arising from their outstanding power density and efficient charge-discharge characteristics [3–5]. $Bi_{0.5}Na_{0.5}TiO_3$ (BNT)-based solid solutions are considered promising host materials for moderate-field dielectric energy storage ceramics [6], owing to their large intrinsic polarization and appropriate Curie temperature [7, 8]. However, pure BNT exhibits certain limitations, such as insufficient breakdown strength (E_b), limited low-field polarization response, and consequently low energy storage efficiency (η) [9, 10], which hinder its ability to meet the rigorous application demands of high-power electronic systems [11]. Previous studies have demonstrated that incorporating $Sr_{0.7}La_{0.2}TiO_3$ (SLT) into BNT to form a binary solid solution effectively perturbs the long-range ferroelectric correlation and triggers the emergence of PNRs [12]. This transformation considerably reduces the remanent polarization and optimizes the *P-E* hysteresis curve, providing a solid basis for enhancing energy storage performance under intermediate electric fields [13, 14]. Nevertheless, the energy storage density of binary BNT-SLT series at moderate fields still requires further improvement. Synergistic optimization via ternary system design is recognized as an effective strategy to concurrently enhance breakdown strength and refine relaxor behavior [15]. As a representative linear dielectric, $CaZrO_3$ (CZ) possesses high electrical resistivity, a low thermal expansion coefficient, and superior structural stability. The incorporation of Ca^{2+} and Zr^{4+} ions into the perovskite A and B sites, separately, induces significant lattice distortion, refines the grain size, and suppresses oxygen vacancy concentration. These synergistic effects collectively elevate the dielectric breakdown strength and modulate the relaxor characteristics of the system [16]. Supporting this approach, research on related systems has shown promising results: Zhang et al. reported that for $0.55Na_{0.5}Bi_{0.5}TiO_3$-$0.45(Sr_{0.7}La_{0.2})(Ti_{0.8}Sn_{0.2})O_3$ ceramics, W_{rec} of approximately 2.52 J/cm³ and an η of about 89.3% were achieved, both of which represent outstanding performance levels [17]. P_{max} of roughly 50μC/cm^2 was attained in 0.76BNT-0.24ST ceramics under a 100 kV/cm field, as reported by Ma et al. Given this substantial polarization response, $0.76Bi_{0.5}Na_{0.5}TiO_3$-$0.24Sr_{0.7}La_{0.2}TiO_3$ serves as the host matrix for the current investigation [18]. Zhao et al. developed zirconium-doped BNT-ST ceramics that achieved W_{rec} of 4.6 J/cm³ and an η of 82% at an electric field of 250 kV/cm. Furthermore, the dielectric properties remained highly stable throughout a wide range of frequencies (1-100 Hz) and temperatures (20–120°C) [19]. Compared to the binary BNSLT, the introduction of Ca^{2+} and Zr^{4+} ions is anticipated to bring synergistic benefits. Consequently, Ca^{2+} and Zr^{4+} ions were introduced into the 0.76BNT-0.24SLT matrix in this study. On this basis, a ternary ceramic system, (1-*x*)($0.76Bi_{0.5}Na_{0.5}TiO_3$-$0.24Sr_{0.7}La_{0.2}TiO_3$)-*x*$CaZrO_3$, was designed and synthesized to systematically investigate the influence of CZ doping on the phase structure, microstructure, dielectric properties, and energy storage performance.

2 Experimental method

Lead-free BNSLT-*x*CZ (*x* = 0.00-0.15) ceramics with varying CZ contents were produced through a classical solid-state sintering process. The raw materials used included Na_2CO_3 (99.8%), $CaCO_3$ (99.0%), Bi_2O_3 (99.7%), $SrCO_3$ (99.0%), La_2O_3 (99.9%), TiO_2 (99.0%), and ZrO_2 (99.0%). Initially, to eliminate

adsorbed moisture, the starting powders underwent a dehydration process at 80°C for 24 h. After weighing in accordance with the calculated molar proportions, the mixture was pulverized via ball milling for 24 h, using anhydrous ethanol as the milling agent.Following the drying process at 80°C, the resultant mixtures were granulated using an 80-mesh sieve and subsequently compacted into green pellets, which were calcined at 830°C over a 4 h period. The calcined samples underwent secondary ball milling, drying, and screening. The resultant powders were fabricated into green disks, processed via cold isostatic pressing (CIP),with the final sintering conducted for 10 h within a temperature range of 1080–1120°C. To identify the crystalline phases of the samples, X-ray diffraction (XRD) patterns were collected using a Bruker D8 Advance diffractometer. To reveal the grain growth and pore distribution, scanning electron microscopy (SEM, JSM 6490LV, Japan) was employed for morphological observation. The dielectric behavior was investigated via a Tonghui TH2826A LCR meter. Polarization-electric field (*P-E*) curves were recorded via an aixACCT TF-2000 ferroelectric test system. A CHI660E electrochemical analyzer was employed to evaluate the electrical impedance behavior of the specimens.

3 Results and discussion

Figure 1(a) the phase evolution and structural characteristics of the (1-*x*)BNSLT-*x*CZ solid solutions at ambient temperature are illustrated through the XRD patterns. As illustrated, the diffraction peaks for all compositions correspond well to the typical perovskite ABO_3 structure [20, 21]. No discernible secondary phase peaks are observed, suggesting that CZ has completely incorporated into the BNSLT lattice to form a stable and homogeneous perovskite solid solution within the range of x = 0.00-0.15 [22, 23]. Figure 1(b) provides a detailed view of the (111) diffraction peaks. The undoped x = 0.00 sample exhibits distinct peak splitting. This splitting is a characteristic signature of a non-cubic structure, indicating that the pristine BNSLT matrix is dominated by a rhombohedral phase with long-range ferroelectric order.With increasing CZ doping concentration, the splitting of the (111) peak gradually diminishes and eventually merges into a single, symmetric, and broadened peak, demonstrating typical pseudocubic phase characteristics [24, 25]. This evolution demonstrates that the incorporation of CZ effectively destabilizes the long-range ferroelectric order, inducing a structural evolution from the rhombohedral phase toward a pseudocubic structure. This process facilitates the evolution of PNRs, therefore establishing a favorable structural foundation for excellent energy storage properties. Furthermore, as the CZ concentration increases, all diffraction peaks shift slightly toward low-angle region. This shift is mainly ascribed to the B-site substitution of Ti^{4+} (0.605 Å) by larger Zr^{4+} (0.72 Å) ions. This ionic replacement induces lattice expansion and an increase in unit cell parameters [26], verifying that a robust BNSLT-*x*CZ solid solution has been established.

Figure 2(a)-(d) presents a representative set of SEM micrographs and grain size statistical data for the BNSLT-*x*CZ series. All BNSLT-*x*CZ ceramics exhibit a dense and homogeneous microstructure, characterized by well-defined grain boundaries and the absence of discernible defects such as pores or cracks. This suggests that the optimized sintering process facilitates the fabrication of highly densified ceramic bodies [27], providing a critical prerequisite for achieving superior electrical performance.The

average grain sizes for the samples with x = 0.00, 0.05, 0.10, and 0.15 are 2.11 μm, 1.65 μm, 1.21 μm, and 1.74 μm, respectively. A clear decreasing trend in grain size is observed as x increases up to 0.10. This grain refinement is mainly ascribed to several factors. First, the entry of Ca^{2+} and Zr^{4+} ions into the perovskite lattice introduces lattice strain energy due to ionic size mismatch, which can impede grain boundary mobility and suppress grain growth during sintering [28, 29]. Second, the incorporation of CZ suppresses the oxygen vacancy level and reduces conduction loss, which hinders the mass transfer process and effectively prevents abnormal grain growth [30]. A further increase in CZ content to x = 0.15 instead promotes the growth of average grains. This reversal may be attributed to the excessive CZ doping, which could exacerbate lattice mismatch and enhance local ionic diffusion, thereby triggering secondary grain growth [31].

As illustrated in the EDS elemental mapping in Fig. 2(e), all matrix and dopant elements (Bi, Na, Ti, Sr, and La) and the dopants (Ca and Zr) are uniformly distributed across the mapped region of the x = 0.10 sample, with no discernible evidence of local segregation or enrichment. These results confirm that a homogeneous elemental dispersion at the micrometer scale has been successfully achieved [32, 33].

Within the frequency spectrum of 1 kHz to 1 MHz, the dielectric properties (ε_r and tanδ) of the BNSLT-xCZ system are depicted in Fig. 3. As illustrated, the distinct features of relaxor ferroelectricity are universally observed across the entire set of compositions. [34, 35]. Specifically, the ε_r initially increases with rising temperature until reaching a maximum T_m, followed by a gradual decrease. Notably, the dielectric peak shifts toward higher temperatures with increasing test frequency, accompanied by a progressive reduction in peak intensity. This frequency-dependent dispersion originates from the thermally activated relaxation behavior of PNRs [36, 37]. With increasing CZ content, the temperature of the dielectric maximum T_m progressively shifts toward lower values. Concurrently, the peak dielectric constant decreases significantly-for instance, A significant reduction in ε_r is observed, falling from 3000 at x = 0.00 to 1050 at x = 0.10.Furthermore, the dielectric peak becomes increasingly broadened and diffuse. These observations collectively indicate a significant enhancement of relaxor characteristics, which aligns perfectly with the XRD analysis. The evolution confirms that CZ doping effectively disrupts the long-range ferroelectric order, stabilizes a pseudocubic structure,and triggers the proliferation of high-density PNRs. As observed from the dielectric loss curves, all samples maintain a low tanδ over a broad temperature span from ambient temperature to 250°C. Notably, in the x = 0.10 composition, the tan δ values remain consistently below 0.05 throughout this entire temperature interval, demonstrating excellent insulation performance. As the temperature exceeds 300°C, the gradual increase in CZ doping effectively suppresses the upsurge of dielectric loss in the elevated temperature range. Such suppression stems from the reduced oxygen vacancy concentration induced by CZ doping, thereby diminishing the associated conduction losses and leakage current at elevated temperatures [38]. Furthermore, the samples with $x \geq 0.10$ exhibit minimal fluctuations (±10%) in dielectric properties throughout a wide temperature and frequency window. This indicates that optimal CZ doping not only enhances the relaxor nature but also substantially enhances the thermal and frequency independence of

the dielectric properties, thereby offering a significant strategic advantage for the deployment of energy storage systems in sophisticated and extreme environments.

Figure 4(a) presents the complex impedance representations for BNSLT-*x*CZ samples with various compositions obtained at 480°C. A single Debye-like semicircular arc is observed for all compositions, reflecting the predominance of a unique electrical contribution at this temperature, which is widely attributed to the grain (bulk) effect [39, 40]. An initial increase followed by a downward trend is observed in the arc radius as the CZ doping concentration scales up. Specifically, the x = 0.10 composition possesses the largest radius, revealing the highest grain resistance and the most optimized bulk dielectric properties among all studied samples. Figure 4(b) shows the impedance response of the x = 0.10 composition within the 460–540°C temperature window. A monotonic reduction in the arc radius is observed as the temperature rises, demonstrating a typical negative temperature coefficient (NTC) thermistor characteristics. Such behavior originates from the thermal activation of oxygen vacancy species and lattice defects with increasing temperature, thereby promoting charge carrier mobility and leading to an enhanced electrical conductivity [41, 42]. Figure 4(c) illustrates the evolution of the Z"/Z"max spectra with frequency for x = 0.10 ceramics, recorded between 420 and 540°C. With increasing temperature, the relaxation peaks shift systematically to higher frequencies, confirming the occurrence of typical thermally stimulated dielectric relaxation process [43]. This evolution is intimately linked to the long-distance migration of defects, particularly oxygen vacancy defects, within the ceramic lattice [44, 45].

Activation energy (E_a) is a fundamental parameter in materials science that characterizes the energy barrier for ionic diffusion, chemical reactions, or charge transport processes. Figure 4(d) presents Arrhenius relationship for log σ as a founction of 1000/T, from which the E_a for electrical conduction is derived using the equation [46]:

$$\sigma = \sigma_c \exp(-E_a/KT)$$

4

where symbols σ and K signify the conductivity and Boltzmann's constant, respectively.The obtained E_a values fall within the interval of 1.422–1.558 eV. As illustrated in Fig. 4(d), the activation energy initially grows with the CZ content, peaking at 1.637 eV for the composition with x = 0.10, followed by a subsequent decrease. It is revealed that a proper CZ content facilitates a more vigorous defect migration and diffusion process, particularly oxygen vacancies. The increased energy barrier at x = 0.10 significantly hinders charge transport, thereby enhancing the insulation resistance and dielectric reliability of the ceramics [47].

Figure 5 the morphological transition of *P-E* hysteresis loops, along with the associated energy storage parameters (W_{rec} and η), are depicted in Figures (a) and (b) for the BNSLT-*x*CZ ceramic series under an applied frequency of 10 Hz. As the concentration of CZ substitution gradually rises, a progressive slenderizing of the *P-E* hysteresis curves is observed, along with a notable enhancement in the W_{rec}

values. The x = 0.10 composition yields the peak W_{rec} value of 2.91 J/cm3, which is accompanied by a storage η of 64.31%. Further increasing x to 0.15 leads to a slight decrease in W_{rec} (~ 2.76 J/cm³), while η continues to rise, reaching 70.53%. Concurrently, both the P_{max} and the P_r exhibit a marked decrease with increasing x. Specifically, P_{max} declines from 51.83 μC/cm² (x = 0.00) to 33.25 μC/cm² (x = 0.15), simultaneously P_r drops sharply from 20.14 μC/cm² to 3.94 μC/cm². The observed manifestation potentially stems from the incorporation of foreign atoms via CZ substitution, which destabilizes the long-range ferroelectric alignment within the BNSLT host and promotes the formation and refinement of PNRs [48, 49]. Compared to conventional macro-domains, these PNRs are characterized by their nanoscale size and high dynamics. They can align rapidly under an applied electric field to yield a moderate P_{max}, yet switch back almost completely upon field removal, resulting in a drastically reduced P_r and a slim *P-E* loop [50]. Concurrently, The gradual decline in P_{max} is attributed to the dilution of the ferroective host (BNT) by the linear dielectric CZ, which inherently possesses a lower polarization capability. This dilution effect tends to suppress the overall spontaneous polarization intensity of the solid solution [51]. Nevertheless, the significant reduction in P_r outweighs the decrease in P_{max} for compositions up to x = 0.10, leading to an enlarged ΔP (= P_{max} - P_r) and, consequently, an enhanced W_{rec}. For x = 0.15, although P_r is further minimized (benefiting η), the more substantial drop in P_{max} causes ΔP and W_{rec} to decrease.

For a more detailed exploration of the energy storage capabilities (ESP) observed by the BNSLT-0.10CZ composition, Fig. 5(c) illustrates the *P-E* hysteresis behavior across a range of electric field intensities. Additionally, Fig. 5(d) illustrates the corresponding evolution of W_{rec} and η versus the applied electric field.As show, the *P-E* curves remain relatively slender, indicating a weak hysteresis effect. As the applied field intensifies, the W_{rec} value rises progressively between 0.19 J/cm³ and 2.48 J/cm³. Concurrently, the η level shows a moderate reduction from 72.60% to 65.46%. The monotonic increase in W_{rec} is primarily driven by the enhanced P_{max} under higher fields, while the P_r remains exceptionally low due to the dominant relaxor behavior. This results in a continuously expanding polarization difference ΔP, which is the key determinant for W_{rec}. The slight decrease in η is commonly observed at elevated fields and can be attributed to a gradual increase in energy loss (W_{loss}), likely associated with minor irreversible domain wall motion or defect-related conduction at high biases. Importantly, the η value remains above 65% throughout the tested field range, underscoring the material's excellent relaxor nature and low-loss characteristics, which are crucial for reliable operation under high fields [52].

For practical engineering applications, energy storage ceramics must possess superior thermal stability and frequency reliability to ensure consistent high performance under complex and demanding operating conditions. Figure 6(a)-(b) illustrates the temperature-related *P-E* curves and the evolution of W_{rec} and η levels for the BNSLT-0.10CZ composition, performed within a thermal window of 30–150°C under an applied field of 180 kV/cm and a 10 Hz frequency. The *P–E* curves retain their narrow profile, relaxor-like profile across the complete thermal span, confirming the stability of the relaxor state [53]. Across the thermal interval of 30–150°C,the W_{rec} value exhibits a subtle increase, moving from 1.53

J/cm³ to 1.66 J/cm³, while the η value increases from 71.2% to 79.79%. The calculated variation rates for W_{rec} and η are less than 5.56% and 6.28%, respectively, indicating outstanding thermal stability.Furthermore, spanning a frequency interval from 5 to 100 Hz, as depicted in (Fig. 6(c)-(d)), the values of W_{rec} and η decrease to 1.47 J/cm³ and 68.85%, starting from 1.61 J/cm³ and 74.35%, respectively., with variation rates below 4.41% and 3.20%, respectively, demonstrating excellent frequency insensitivity. This robust stability is primarily attributed to the inherent relaxor characteristics of the material, alongside the rapid dynamic response and high thermal stability of the PNRs [54, 55].

4 Conclusion

The (1-*x*)BNSLT-*x*CZ compositions investigated in this work were processed using the classical solid-state ceramic route. This study systematically evaluated how $CaZrO_3$ (CZ) addition modulates the structural evolution and microstructure, as well as the resulting dielectric response, impedance properties, and energy storage capabilities. Driven by the development of a single-phase perovskite lattice in the BNSLT matrix, CZ doping inhibits long-range ferroelectric ordering. The resulting multiphase coexistence and PNRs density significantly optimize the dielectric relaxation properties. Appropriate CZ incorporation contributes to grain refinement and densification, with a concurrent rise in the carrier activation energy E_a, which collectively improves the dielectric performance. Superior energy storage performance is attained specifically when x = 0.10, where a W_{rec} of 2.91 J/cm³ and an η of 64.3% are achieved at an electric field of 230 kV/cm. Moreover, the ceramic demonstrates excellent temperature stability, with the fluctuations of W_{rec} and η staying within 5.56% and 6.28%, respectively, throughout the thermal span of 30–150°C. The x = 0.10 sample maintains remarkable consistency over a broad frequency window (5–100 Hz), as evidenced by the small variation amplitudes (below 4.41% for W_{rec} and 3.20% for η). To conclude, the BNSLT-0.10CZ ceramic delivers a compelling combination of high energy density and exceptional environmental reliability, even at moderate electric field levels. This lead-free dielectric candidate exhibits great promise for microelectronic integration and offers critical experimental and theoretical frameworks for advancing high-performance energy storage ceramics.

Declarations

The authors declare that they have no known competing financial interests or personal relationships that could have appeared to influence the work reported in this paper.

Acknowledgements

This work is partly supported by the Research Project of Natural Science in Anhui Higher Education Institutions (No. 2023AH051372; 2025AHGXZK20008; 2025AHGXZK30189), the Key Project of Anhui Provincial Power Integrated Circuit Engineering Research Center (No.ERCPZX202403), and open research project Engineering Technology Research Center of Intelligent Microsystems Anhui Province (No.ETRCIM202504).

Conflict of interest

The authors declare no conflict of interest regarding the publication of this paper.

Competing Interests

The authors have no relevant financial or non-financial interests to disclose.

Author Contributions statement

Xiaofan Zheng: Writing - original draft, Formal analysis, Data curation. Shuyue Teng: Writing - review & editing, Investigation. Chong Li: Investigation, Supervision. Shuyue Teng : Formal analysis, Data curation. Mile Wei: software, resources. Juan Hu: Conceptualization, Funding acquisition, Investigation. Huanghuang Jin: Project administration. Huanghuang Jin: Supervision, Funding acquisition. Qin Gao: Validation, Methodology.

Research Data Policy and Data Availability Statements

The datasets generated during and/or analysed during the current study are available from the corresponding author on reasonable request.

References

1. Q. Gao, N. Zhao, W. Zhang et al., Ceram. Int. **51**, 64867–64879 (2025). https://doi.org/10.1016/j.ceramint.2025.11.020
2. X. Zhong, Y. Chen, A. Shui et al., J. Mater. Sci.: Mater. Electron. **34**, 1002 (2023). https://doi.org/10.1007/s10854-023-10300-5
3. H. He, X. Lu, M. Li et al., J. Mater. Chem. C **8**, 2411–2418 (2020). https://doi.org/10.1039/c9tc04864b
4. C. Zhu, Z. Cai, B. Luo et al., ACS Appl. Mater. Interfaces. **13**, 28484–28492 (2021). https://doi.org/10.1021/acsami.1c06075
5. H. Wen, X. Wu, Z. Jin et al., J. Mater. Sci.: Mater. Electron. **35**, 633 (2024). https://doi.org/10.1007/s10854-024-12403-z
6. M. Wang, Q. Feng, C. Luo et al., ACS Appl. Mater. Interfaces. **13**, 51218–51229 (2021). https://doi.org/10.1021/acsami.1c14151
7. X. Li, X. Dong, F. Wang et al., J. Eur. Ceram. Soc. **42**, 2221–2229 (2022). https://doi.org/10.1016/j.jeurceramsoc.2021.12.028

8. X. Liu, H. Du, X. Liu et al., Ceram. Int. **42**, 17876–17879 (2016). https://doi.org/10.1016/j.ceramint.2016.08.087
9. S. Bian, Z. Yue, Y. Shi et al., J. Am. Ceram. Soc. **104**, 936–947 (2020). https://doi.org/10.1111/jace.17486
10. L. Zhang, Y. Pu, M. Chen et al., J. Eur. Ceram. Soc. **41**, 5890–5899 (2021). https://doi.org/10.1016/j.jeurceramsoc.2021.05.036
11. G. Liu, H. Fan, J. Shi et al., Ceram. Int. **42**, 3938–3946 (2016). https://doi.org/10.1016/j.ceramint.2015.11.062
12. J. Hu, N. Zhao, L. Ding et al., Ceram. Int. **51**, 11974–11981 (2025). https://doi.org/10.1016/j.ceramint.2025.01.049
13. C. Long, T. Du, W. Ren, J. Mater. Sci. **55**, 5715–5729 (2020). https://doi.org/10.1007/s10853-020-04431-x
14. X. Zhao, W. Bai, Y. Ding et al., J. Eur. Ceram. Soc. **40**, 4475–4486 (2020). https://doi.org/10.1016/j.jeurceramsoc.2020.05.078
15. R. Kumari, N. Ahlawat, A. Agarwal et al., J. Alloys Compd. **676**, 452–460 (2016). https://doi.org/10.1016/j.jallcom.2016.03.088
16. M. Lun, W. Wang, Z. Xing et al., J. Am. Ceram. Soc. **102**, 5243–5252 (2019). https://doi.org/10.1111/jace.16394
17. X. Zhang, F. Yang, W. Miao et al., J. Alloys Compd. **883**, 160837 (2021). https://doi.org/10.1016/j.jallcom.2021.160837
18. W. Ma, Y. Zhu, M.A. Marwat et al., J. Mater. Chem. C **7**, 281–288 (2019). https://doi.org/10.1039/c8tc04447c
19. N. Zhao, L. Jiang, X. Zheng et al., J. Mater. Sci. **60**, 2464–2477 (2025). https://doi.org/10.1007/s10853-024-10587-7
20. N. Zhao, X. Zheng, F. Huang et al., Ceram. Int. **50**, 8325–8331 (2024). https://doi.org/10.1016/j.ceramint.2023.12.166
21. D. You, H. Tan, Z. Yan et al., ACS Appl. Mater. Interfaces. **14**, 17652–17661 (2022). https://doi.org/10.1021/acsami.2c01406
22. G.-D. Zhang, J.-Q. Dai, G.-Y. Zhang et al., J. Mater. Sci.: Mater. Electron. **33**, 10226–10233 (2022). https://doi.org/10.1007/s10854-022-08011-4
23. F. Zhang, Z. Dai, Y. Pan et al., Int. J. Energy Res. **46**, 11492–11500 (2022). https://doi.org/10.1002/er.7897
24. X. Nie, Y. He, Q. Shi et al., J. Adv. Dielectr. **13**, 2242005 (2023). https://doi.org/10.1142/s2010135x2242005x
25. Y. Yang, J. Xu, L. Yang et al., Mater. Chem. Phys. **276**, 125402 (2022). https://doi.org/10.1016/j.matchemphys.2021.125402

26. M.-Y.T. Yang Li, Z.-G. Zhang, Q. Li, J.-L. Li, G.L. Zhuo, F. Xu, Li, Rare Met. **42**, 1261–1273 (2022). https://doi.org/10.1007/s12598-022-02175-y
27. Z. Wang, R. Kang, W. Liu et al., Chem. Eng. J. **427**, 131989 (2022). https://doi.org/10.1016/j.cej.2021.131989
28. X. Zhou, Z. Yan, H. Qi et al., J. Eur. Ceram. Soc. **39**, 2310–2317 (2019). https://doi.org/10.1016/j.jeurceramsoc.2019.02.008
29. X. Qiao, D. Wu, F. Zhang et al., J. Mater. Chem. C **7**, 10514–10520 (2019). https://doi.org/10.1039/c9tc03597d
30. J. Wang, F. Zhang, Z. Peng et al., J. Materiomics. **8**, 1077–1085 (2022). https://doi.org/10.1016/j.jmat.2022.02.003
31. J. Ye, Y. Liu, Y. Lu et al., J. Mater. Sci.: Mater. Electron. **25**, 4632–4637 (2014). https://doi.org/10.1007/s10854-014-2215-5
32. X. Wang, Y. Huan, S. Ji et al., Nano Energy. **101**, 107580 (2022). https://doi.org/10.1016/j.nanoen.2022.107580
33. T. Zheng, Z. Jiang, J. Wu, Dalton Trans. **45**, 11277–11285 (2016). https://doi.org/10.1039/c6dt01805j
34. X. Liu, H. Yang, F. Yan et al., J. Alloys Compd. **778**, 97–104 (2019). https://doi.org/10.1016/j.jallcom.2018.11.106
35. J. Xie, Z. Dai, X. Ding et al., J. Mater. Sci. **55**, 13578–13589 (2020). https://doi.org/10.1007/s10853-020-04978-9
36. R. Dou, L. Yang, J. Xu et al., Mater. Res. **22** (2019). https://doi.org/10.1590/1980-5373-mr-2018-0720
37. H. Wang, H. Yuan, X. Li et al., Chem. Eng. J. **394**, 124879 (2020). https://doi.org/10.1016/j.cej.2020.124879
38. M. Ullah, A. Ullah, H.U. Khan et al., J. Korean Phys. Soc. **76**, 145–149 (2020). https://doi.org/10.3938/jkps.76.145
39. S. Lu, N. Zhao, K. Song et al., Mater. Today Commun. **42**, 111438 (2025). https://doi.org/10.1016/j.mtcomm.2024.111438
40. X. Liu, H. Fan, J. Shi et al., RSC Adv. **6**, 30623–30627 (2016). https://doi.org/10.1039/c6ra00682e
41. Z. Song, H. Liu, H. Hao et al., IEEE Trans. Ultrason. Ferroelectr. Freq. Control. **62**, 609–616 (2015). https://doi.org/10.1109/TUFFC.2014.006927
42. H. Tian, H. Fan, G. Dong et al., RSC Adv. **6**, 109091–109098 (2016). https://doi.org/10.1039/c6ra19520b
43. T. Wang, J. Hu, H. Yang et al., J. Appl. Phys. **121**, 084103 (2017). https://doi.org/10.1063/1.4977107
44. J. Shi, H. Fan, X. Liu et al., J. Alloys Compd. **627**, 463–467 (2015). https://doi.org/10.1016/j.jallcom.2014.12.022
45. G. Liu, H. Fan, G. Dong et al., J. Alloys Compd. **664**, 632–638 (2016). https://doi.org/10.1016/j.jallcom.2015.12.260

46. N. Zhao, H. Fan, L. Ning et al., J. Am. Ceram. Soc. **101**, 5578–5585 (2018). https://doi.org/10.1111/jace.15870
47. L. Wu, X. Wang, L. Li, RSC Adv. **6**, 14273–14282 (2016). https://doi.org/10.1039/C5RA21261H
48. X. Chen, X. Gong, T. Li et al., J. Alloys Compd. **507**, 535–541 (2010). https://doi.org/10.1016/j.jallcom.2010.08.012
49. L. Wu, Y. Yang, S. Zhu et al., J. Mater. Sci.: Mater. Electron. **30**, 200–211 (2018). https://doi.org/10.1007/s10854-018-0282-8
50. S. Zheng, Q. Li, Y. Chen et al., J. Alloys Compd. **911**, 165019 (2022). https://doi.org/10.1016/j.jallcom.2022.165019
51. J. Wang, J.B. Neaton, H. Zheng et al., 299 1719–1722 (2003). https://doi.org/10.1126/science.1080615
52. A.R. Jayakrishnan, J.P.B. Silva, K. Kamakshi et al., Prog. Mater. Sci. **132**, 101046 (2023). https://doi.org/10.1016/j.pmatsci.2022.101046
53. X. Fan, P. Li, J. Du et al., J. Mater. Sci.: Mater. Electron. **31**, 9974–9981 (2020). https://doi.org/10.1007/s10854-020-03602-5
54. Z. He, S. Shi, Z. Pan et al., Ceram. Int. **47**, 11611–11617 (2021). https://doi.org/10.1016/j.ceramint.2020.12.294
55. X. Chen, X. Li, J. Sun et al., Ceram. Int. **46**, 2764–2771 (2020). https://doi.org/10.1016/j.ceramint.2019.09.265

Figures

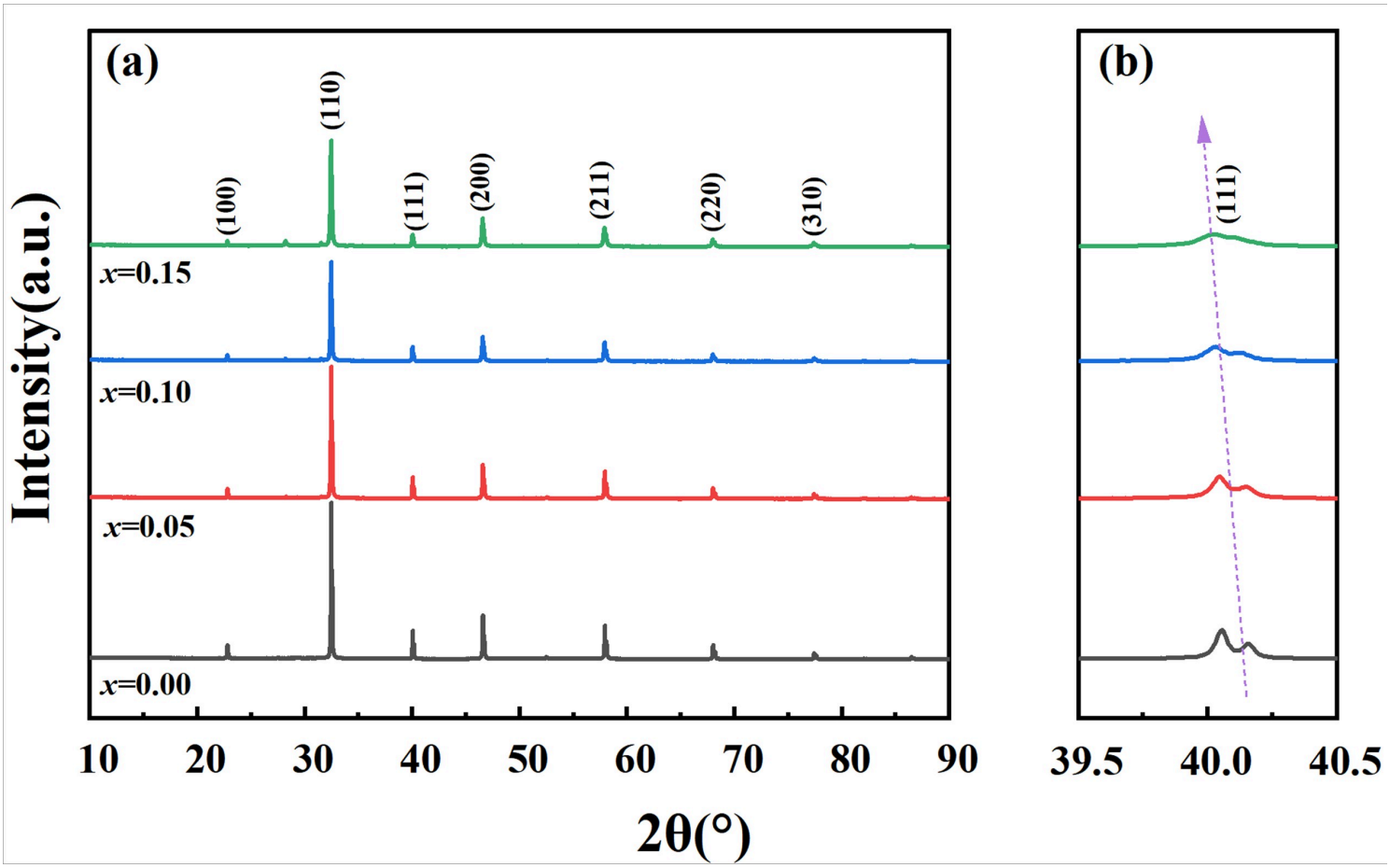


Figure 1

(a) XRD diffractograms of BNSLT-*x*CZ ceramics; (b) Magnified XRD patterns of the (111) peaks.

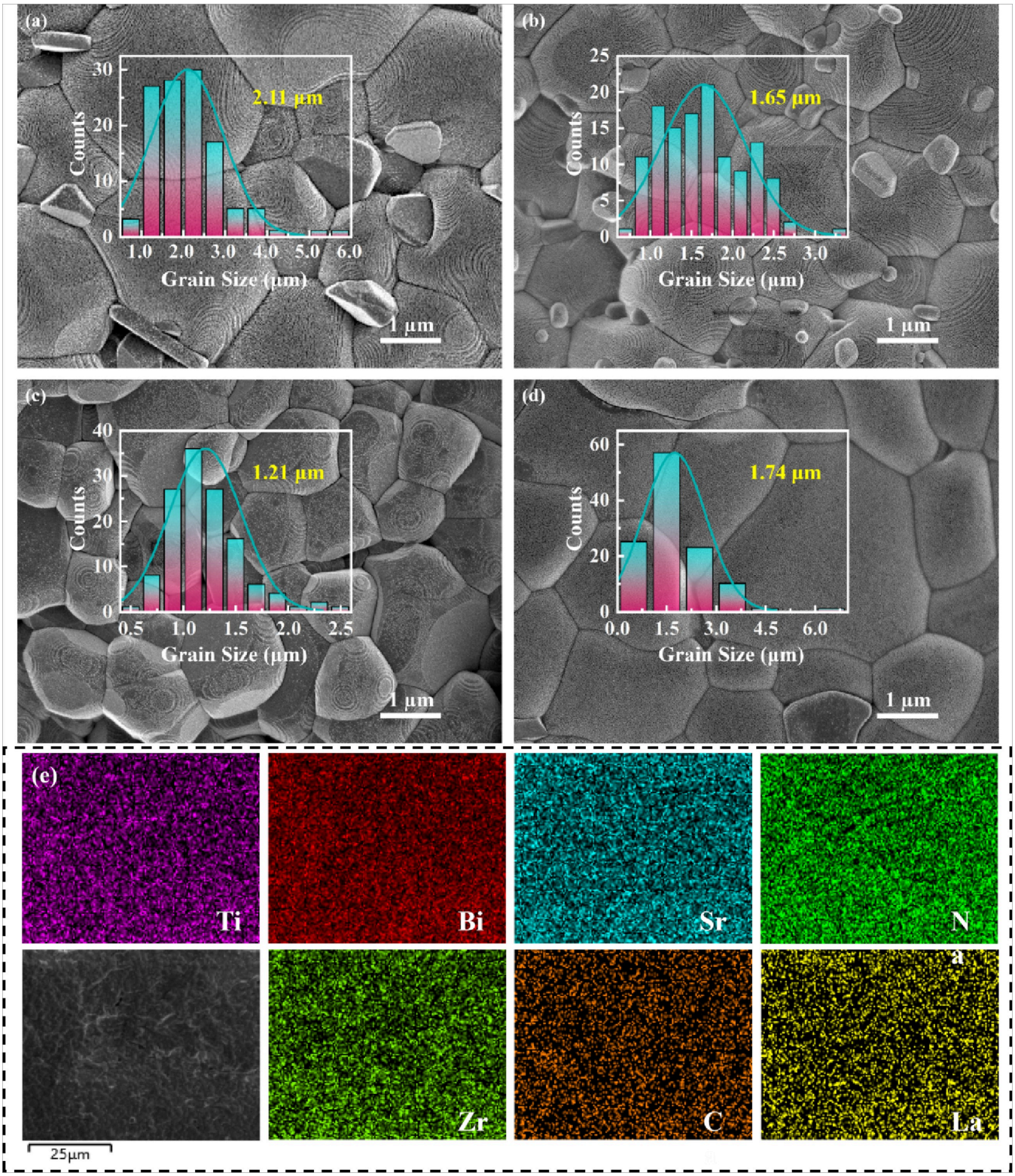


Figure 2

SEM characterization and quantitative grain size analysis of BNSLT-*x*CZ ceramics: (a)-(d) EDS mappings of different compositions (*x* = 0.00-0.15), and (e) for the 0.90BNSLT-0.10CZ ceramic.

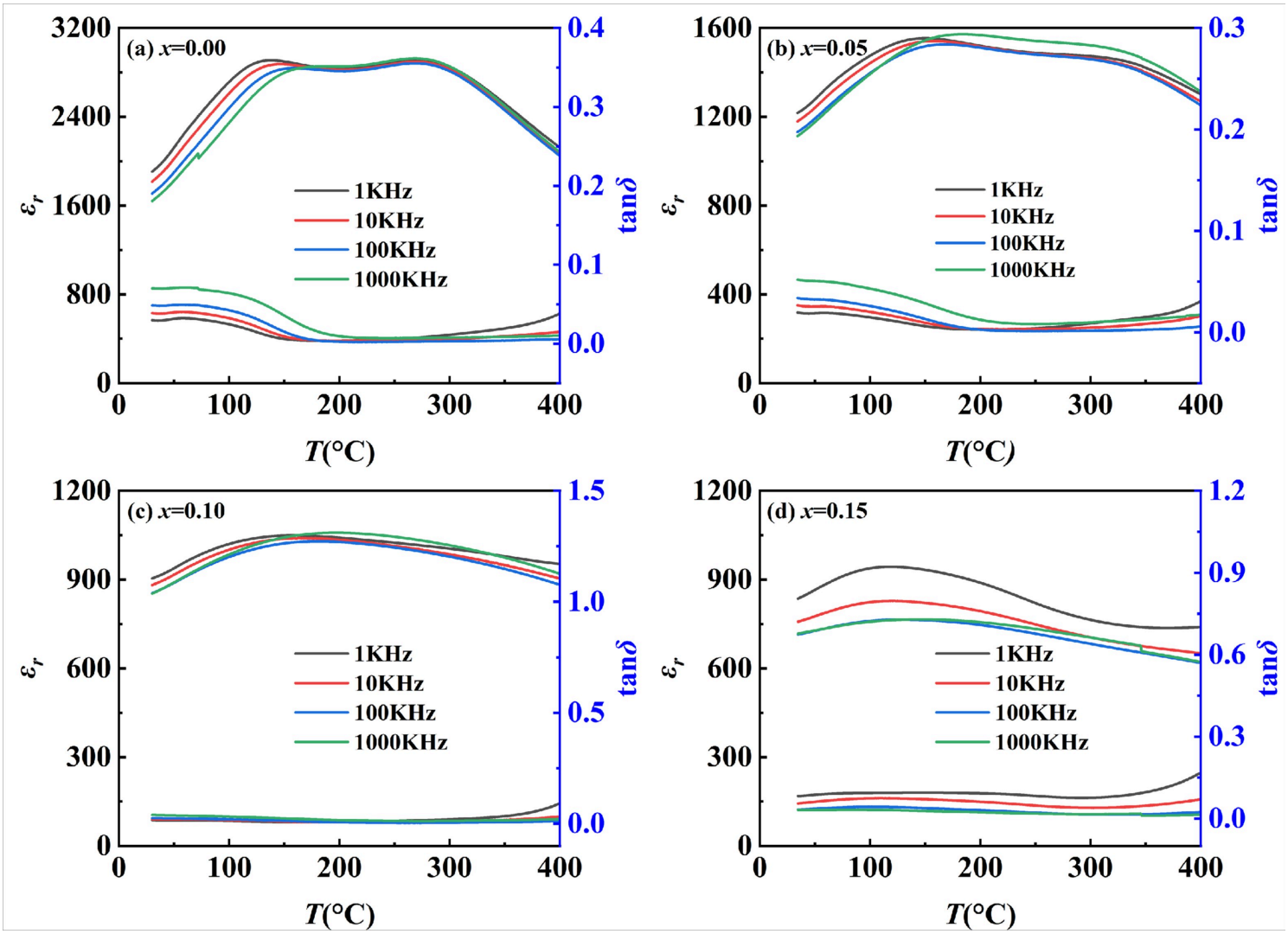


Figure 3

(a)-(d) show the dielectric temperature spectra (ε_r and tanδ) of BNSLT-*x*CZ ceramics tested at frequencies ranging from 1 kHz to 100 kHz, corresponding to doping levels of 0.00, 0.05, 0.10, and 0.15, respectively.

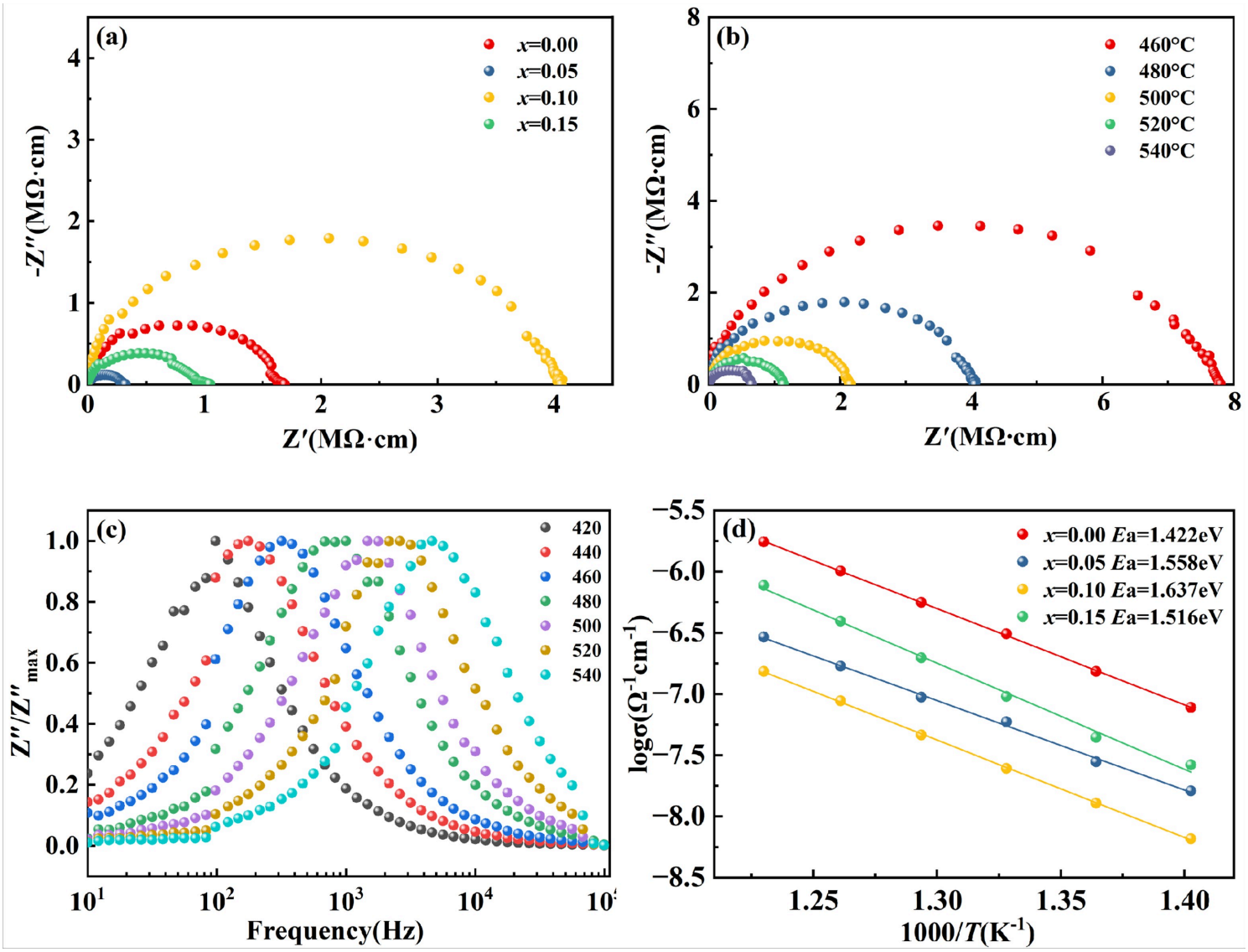


Figure 4

(a) behavior of BNSLT-*x*CZ samples with different CZ doping levels at 480 °C; (b) Impedance behavior of the *x* = 0.10 sample composition within the temperature interval of 460–540 °C; (c) *Z″* spectroscopic plots of the *x*= 0.10 composition across the temperature range 420–540 °C. (d) Relationship between logσ and 1000/T for different CZ doping levels.

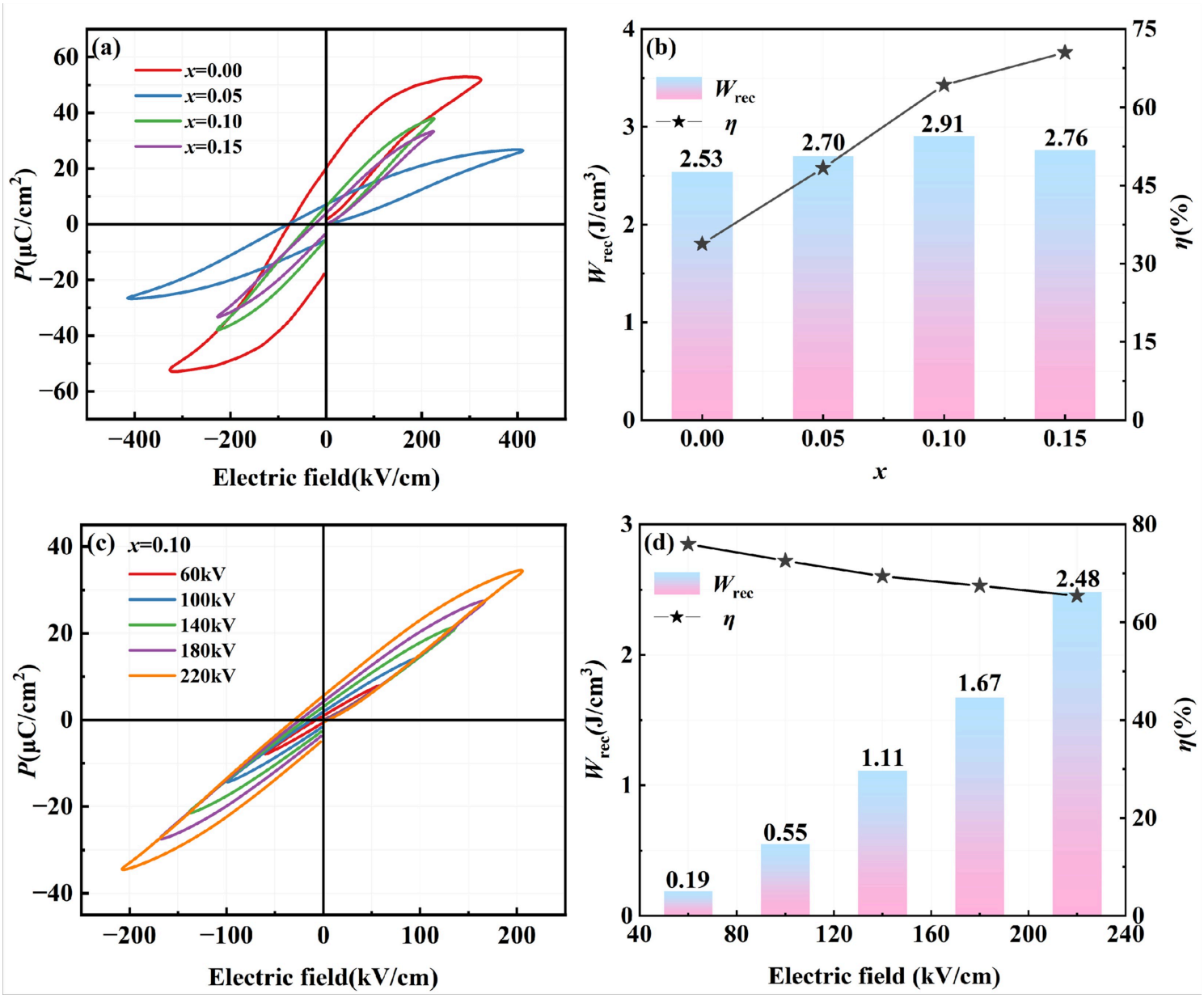


Figure 5

(a)-(d) show, respectively: (a) *P-E* hysteresis characteristics for BNSLT-*x*CZ with varying CZ contents are shown. (b) W_{rec} and η for each group; (c) *P-E* hysteresis at various electric fields; (d) trends in P_{max}, P_r, and P_{max}-P_r.

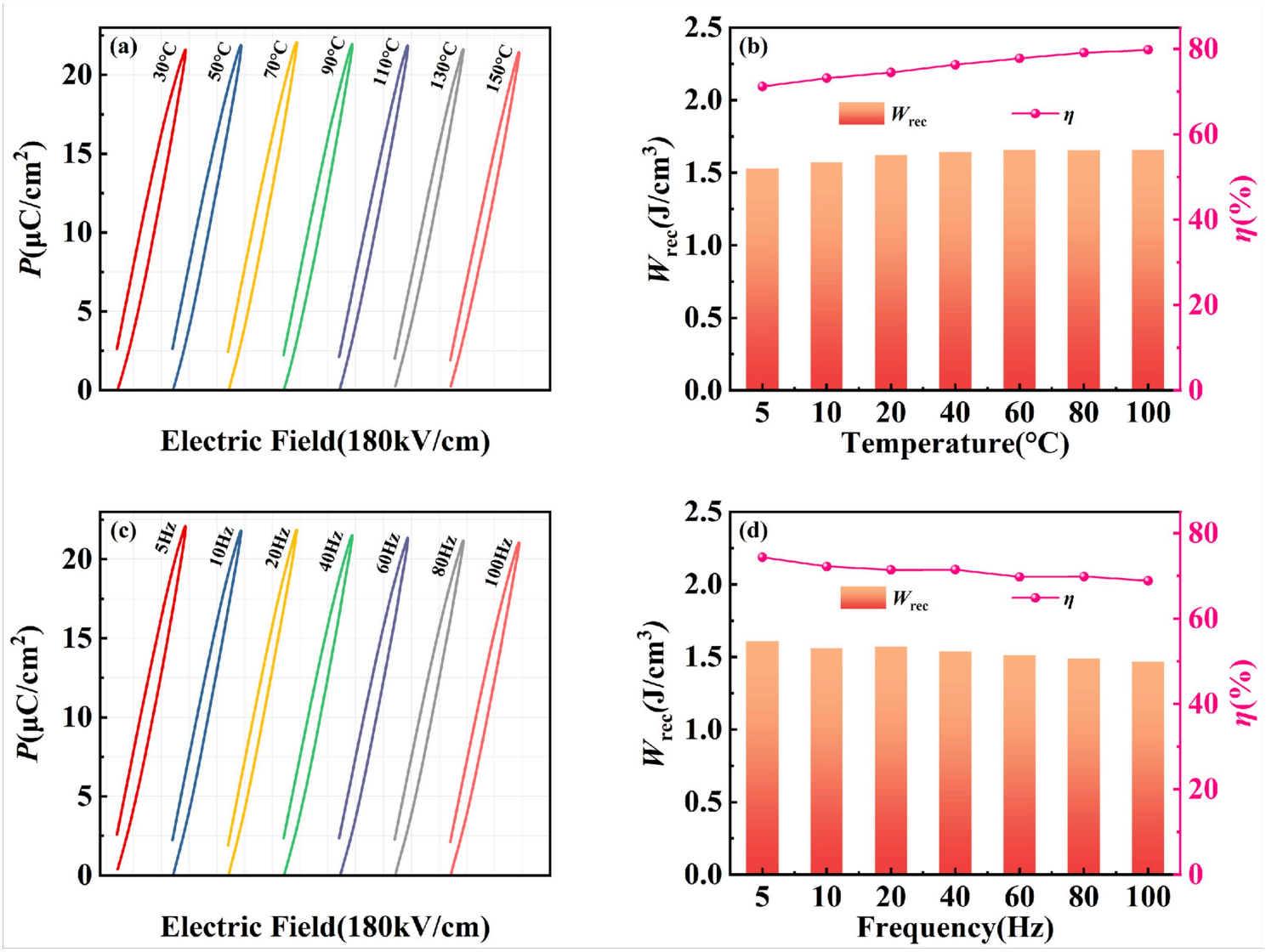


Figure 6

(a) and (b) illustrates the temperature-dependent *P-E* loops along with the corresponding W_{rec} and η values for the BNSLT-0.10CZ specimen over 30–150 °C; (c) and (d) illustrates the frequency-dependent *P-E* loops and the corresponding variation of W_{rec} against η for the specimen over 5–100 Hz.